

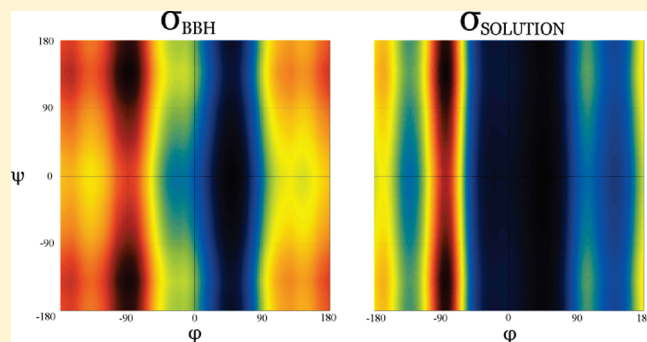
# Using $J$ -Coupling Constants for Force Field Validation: Application to Hepta-alanine

Panagiota S. Georgoulia and Nicholas M. Glykos\*

Department of Molecular Biology and Genetics, Democritus University of Thrace, University Campus, 68100 Alexandroupolis, Greece

Supporting Information

**ABSTRACT:** A computational solution to the protein folding problem is the holy grail of biomolecular simulation and of the corresponding force fields. The complexity of the systems used for folding simulations precludes a direct feedback between the simulations and the force fields, thus necessitating the study of simpler systems with sufficient experimental data to allow force field optimization and validation. Recent studies on short polyaniline peptides of increasing length (up to penta-alanine) indicated the presence of a systematic deviation between the experimental (NMR-derived)  $J$ -couplings and the great majority of biomolecular force fields, with the  $\chi^2$  values for even the best-performing force fields being in the 1.4–1.8 range. Here we show that by increasing the number of residues to seven and by achieving convergence through an increase of the simulation time to 2  $\mu$ s, we can identify one force field (the AMBER99SB force field, out of the three force fields studied) which when compared with the experimental  $J$ -coupling data (and for a specific set of Karplus equation parameters and estimated  $J$ -coupling errors previously used in the literature) gave a value of  $\chi^2 = 0.99$ , indicating that full statistical consistency between experiment and simulation is feasible. However, and as a detailed analysis of the effects of estimated errors shows, the  $\chi^2$  values may be unsuitable as indicators of the goodness of fit of the various biomolecular force fields.



## 1. INTRODUCTION

Short polyaniline peptides are, due to their simplicity, one of the favorite systems used for the optimization and validation of biomolecular force fields.<sup>1–13</sup> In their seminal contribution Graf et al.<sup>7</sup> meticulously measured experimental  $J$ -couplings of a series of polyaniline peptides and compared them (through the application of the Karplus equation<sup>14</sup>) with those derived from molecular dynamics simulations performed with the GROMOS<sup>15</sup> force field. Best et al.<sup>9</sup> and Wickstrom et al.<sup>11</sup> took this further by comparing Graf's experimental data<sup>7</sup> on penta-alanine with a series of different force fields. These studies showed that even the best-performing force fields gave  $\chi^2$  values (comparing experimental and simulation-derived  $J$ -couplings) in the range of 1.4–1.8. This statistically significant deviation between experiment and simulation was interpreted as an indication for the presence of a systematic bias in the force fields' secondary structure preferences<sup>7,9,11</sup> and resulted in various empirical corrections being discussed, with most of them based on a reweighting of the molecular dynamics-derived populations.<sup>7,9</sup> Clearly, the apparent need for an a posteriori correction to the molecular dynamics-derived trajectories is highly unsatisfactory and creates doubts concerning the ability of mainstream nonpolarizable biomolecular force fields to reproduce the experimentally accessible physical reality for even the simpler systems.

To test the hypothesis that the observed deviation between experiment and simulation is partly due to the short length of the pentapeptide combined with the effect of the charges present on its termini,<sup>4,9</sup> we performed molecular dynamics simulations of hepta-alanine in explicit solvent and with full (PME-based<sup>16</sup>) electrostatics and compared the simulation-derived  $J$ -couplings with the experimental values reported by Graf et al.<sup>7</sup> Furthermore, and to convincingly demonstrate that sufficient sampling has been attained, we performed 2  $\mu$ s long simulations with the convergence criterion being the actual  $\chi^2$  values between experiment and simulations. Finally, and to allow a direct comparison with the work of Graf et al.,<sup>7</sup> Best et al.,<sup>9</sup> and Wickstrom et al.,<sup>11</sup> we simulated the hepta-alanine system using three different biomolecular force fields. In the following paragraphs we describe the simulation protocol and analyses performed and compare the results obtained from the three force fields with the experimental findings. This is followed by a critical (almost skeptical) evaluation of problems arising from the uncertainty surrounding the estimation of errors of the calculated  $J$ -couplings and from the asymmetric (for the  $\varphi$  vs  $\psi$  angles) information content of the experimental data. We conclude by discussing possible interpretations of these results.

Received: October 5, 2011

Revised: November 15, 2011

Published: November 16, 2011

## 2. METHODS

### 2.1. Force Fields, System Preparation, and Simulation Protocol.

The three force fields used in our simulations are the CHARMM<sup>17</sup> force field (version c36a2) with the CMAP correction,<sup>18</sup> the OPLS-AA force field,<sup>19,20</sup> and the AMBER99SB force field.<sup>6,11</sup> These will be hereafter referred to as the CHARMM, OPLS, and AMBER force fields. In summary, the system preparation procedure and simulation protocol were as follows. The starting hepta-alanine structure was in the fully extended state as obtained from the program Ribosome (<http://www.roselab.jhu.edu/~raj/Manuals/ribosome.html>). For both the CHARMM and OPLS force fields missing hydrogen atoms were built with the program PSFGEN from the NAMD distribution<sup>21</sup> and solvation–ionization were performed with VMD.<sup>22</sup> In the case of AMBER, system preparation was performed with the program XLEAP from the AMBER tools distribution.<sup>23</sup> The peptide termini were unprotected in agreement with the experimental and simulation conditions previously reported.<sup>7,9,11</sup> For all three force fields we used the TIP3 water model and a cubic unit cell sufficiently large to guarantee a minimum separation between the PBC-related images of the peptide of at least 16 Å.

We followed the dynamics of the three simulations using the program NAMD<sup>21</sup> for a grand total of 6  $\mu$ s (2  $\mu$ s for each force field) as follows: The systems were first energy-minimized for 1000 conjugate gradient steps followed by a slow heating-up phase to a final temperature of 298 K (with a temperature step of 20 K) over a period of 32 ps. Subsequently, the systems were equilibrated for 10 ps under NpT conditions without any restraints, until the volume equilibrated. This was followed by the production NpT run with the temperature and pressure controlled using the Nosé–Hoover Langevin dynamics and Langevin piston barostat control methods as implemented by the NAMD program<sup>21</sup> (and maintained at 298 K and 1 atm). The Langevin damping coefficient was set to 1 ps<sup>-1</sup>, and the piston's oscillation period to 200 fs, with a decay time of 100 fs. The production run was performed with the impulse Verlet-I multiple time step integration algorithm as implemented by NAMD.<sup>21</sup> The inner time step was 2 fs, short-range nonbonded interactions were calculated every one step, and long-range electrostatics interactions every two time steps using the particle mesh Ewald method<sup>16</sup> with a grid spacing of approximately 1 Å and a tolerance of 10<sup>-6</sup>. A cutoff for the van der Waals interactions was applied at 8 Å through a switching function, and SHAKE (with a tolerance of 10<sup>-8</sup>) was used to restrain all bonds involving hydrogen atoms. Trajectories were obtained by saving the atomic coordinates of the whole system every 0.8 ps.

**2.2. Trajectory Analysis.** The program CARMA<sup>24</sup> together with custom scripts were used for most of the analyses, including calculation of torsion angles, calculation of  $J$ -couplings, calculation of  $\chi^2$  values, dihedral space principal component analysis,<sup>25,26</sup> and corresponding cluster analysis, etc. Secondary structure assignments were calculated with the programs STRIDE<sup>27</sup> and DSSP.<sup>28,29</sup> For all analyses the whole trajectories (following the heating-up phase) were used. This is fully justifiable given the very fast equilibration of the systems away from the starting (fully extended) structure. For example, it took only 155 and 121 ps of simulation time before the AMBER- and CHARMM-derived structures are fully in the PPII region (and away from the starting all- $\beta$  structure).

**2.3. Karplus Parameters and Estimated Errors.** Following the work of Graf et al.,<sup>7</sup> Best et al.,<sup>9</sup> and Wickstrom et al.,<sup>11</sup> we

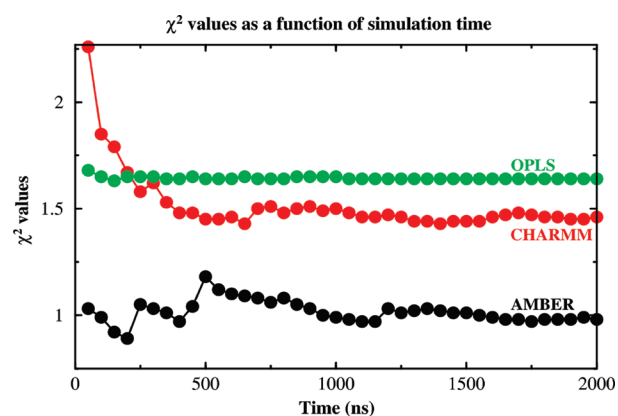


**Figure 1.** Sufficient sampling and convergence: variation of the  $\chi^2$  values for the three force fields as a function of simulation time. For this calculation we have used the DFT1 Karplus parameter set with the  $\sigma_{\text{BBH}}$  error set (see section 2.3 for details). Note the extremely fast convergence of OPLS-AA and the significant fluctuations for the other two force fields reaching out to approximately 1.2  $\mu$ s of simulation time before convergence is achieved.

have used the three different sets of Karplus parameters as reported and used by these authors.<sup>7,9,11,30–34</sup> To maintain consistency with the literature we will keep the Best et al.<sup>9</sup> nomenclature, and we will also refer to these parameter sets as ORIG (Table S2 from Graf et al.,<sup>7</sup> Table S1 from Best et al.,<sup>9</sup> Table S1 from Wickstrom et al.<sup>11</sup>), DFT1 (Table S2 from Best et al.,<sup>9</sup> Table S2 from Wickstrom et al.<sup>11</sup>), and DFT2 (Table S3 from Best et al.,<sup>9</sup> Table S3 from Wickstrom et al.<sup>11</sup>).

We have used three different sets of estimated errors of the Karplus-derived  $J$ -couplings. The first set is the one used by Best et al.<sup>9</sup> and Wickstrom et al.<sup>11</sup> as reported in Table S4 of Wickstrom et al.<sup>11</sup> We will refer to this error set as  $\sigma_{\text{BBH}}$ . The second set is the “X-ray” error set as reported by Hu and Bax<sup>30</sup> in their Table 2 and quoted on Table S4 of Best et al.<sup>9</sup> This will be referred to as the  $\sigma_{\text{X-RAY}}$  error set. The last set is the “solution” error set as reported by Hu and Bax<sup>30</sup> in their Table 2 and will be referred to as  $\sigma_{\text{SOLUTION}}$ .

### 2.4. Error Set Visualization through Reverse Monte Carlo.

The aim of this procedure is to map on the  $(\varphi, \psi)$  plane the constraints imposed by the different Karplus equation error sets. This calculation (whose results are depicted in Figure 3 and discussed in section 3.3) was performed using a custom computer program encoding the following algorithm: (1) initialize the values of the  $(\varphi, \psi)$  distribution map to zero, (2) obtain uniformly random values for the  $(\varphi_i, \psi_i)$  angles of each and every of the  $i$  residues, (3) use the DFT1 parameter set and the  $(\varphi_i, \psi_i)$  angles from the previous step to calculate expected  $J$ -coupling values, (4) assuming a normal distribution, calculate the log(probability) for observing each specific  $J$ -coupling using the error set under study ( $\sigma_{\text{BBH}}$  or  $\sigma_{\text{SOLUTION}}$ ), (5) take the sum of these logarithms, (6) increase the value of the distribution map at each of the  $(\varphi_i, \psi_i)$  points by adding the value of the sum of the logarithms calculated at the previous step, and (7) obtain (randomly) a new set of  $(\varphi_i, \psi_i)$  angles for each an every residue and reiterate for a given number of moves starting from step 3 above.

## 3. RESULTS

**3.1. Sufficient Sampling and Convergence.** Figure 1 shows the variation of the cumulative  $\chi^2$  values as a function of

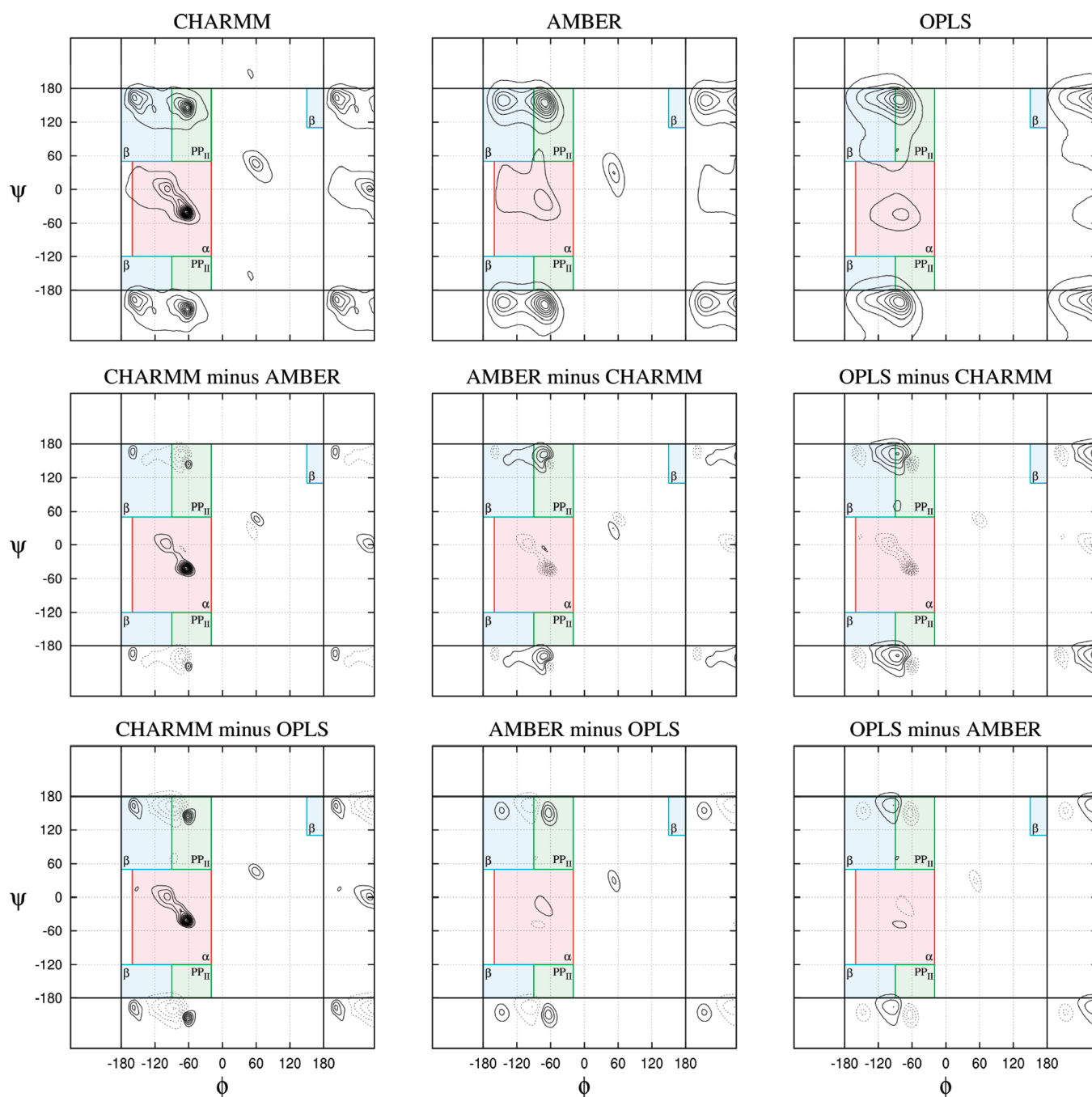


**Figure 2.** Ramachandran and difference Ramachandran plots. The diagrams on the top row show the cumulative Ramachandran plots for each force field [only residues 2–6 (inclusive) have been used for these calculations]. The other two rows correspond to the respective difference maps as noted in their headers. In the difference maps negative contours are drawn with dotted lines. The cumulative diagrams are normalized such that the sum of their respective densities is constant. Contour lines (both positive and negative) are drawn at the same (arbitrary) interval. The  $\alpha$ ,  $\beta$ , and polyproline (PPII) Ramachandran regions are also shown using the definitions given by Best et al. (ref 9).

simulation time for the three force fields studied (the graphs shown in this figure were calculated using the DFT1– $\sigma_{\text{BBH}}$  combination of parameters and error sets; see section 2.3 for definitions). Clearly, the relatively long simulation times we used were necessary (and probably sufficient) for guarantying convergence of the reported statistics. As an example of the relatively slow convergence of the simulations we note that the AMBER force field gave  $\chi^2$  values ranging from almost 0.5 (at  $\sim 250$  ns), to 1.4 (at  $\sim 500$  ns), to a value of 1.0 upon convergence

(which is stably reached after almost 1.2  $\mu\text{s}$  of simulation time). Similar significant fluctuations are also evident for the CHARMM force field, whereas OPLS is the exception having converged within the first 250 ns of the simulation. The same conclusions concerning the convergence behavior of the simulations can be drawn from any of the other parameter–error set combinations (see Supporting Information Figure S1 for the corresponding graphs). The variation of the  $\chi^2$  values as a function of simulation time is not due to the presence of

**Table 1.** Full Set of  $\chi^2$  Values Observed for Each of the Three Force Fields Studied and Each of the Different Sets of Karplus Equation Parameter Sets (ORIG, DFT1, DFT2) and Error Sets ( $\sigma_{\text{BBH}}$ ,  $\sigma_{\text{X-RAY}}$ ,  $\sigma_{\text{SOLUTION}}$ ; See Section 2.3 for Parameter and Error Set Definitions)<sup>a</sup>

force fields	parameter set			error set
	ORIG	DFT1	DFT2	
AMBER	<b>1.56</b>	<b>0.99</b>	<b>1.41</b>	$\sigma_{\text{BBH}}$
	1.43	0.73	1.00	
	1.73	1.47	1.60	
CHARMM	1.77	1.45	1.39	
	1.92	1.65	2.30	
OPLS	1.43	0.96	1.25	
	<b>2.53</b>	<b>1.56</b>	<b>2.28</b>	
AMBER	2.30	1.11	1.56	
CHARMM	2.47	2.03	2.25	
CHARMM	2.45	1.92	1.82	
	2.47	2.03	2.25	
OPLS	3.15	2.71	3.81	
	2.32	1.53	2.02	
AMBER	<b>5.31</b>	<b>3.47</b>	<b>5.04</b>	$\sigma_{\text{SOLUTION}}$
	4.07	1.73	2.33	
CHARMM	4.54	3.73	4.32	
CHARMM	3.85	2.87	2.40	
	7.51	6.86	9.60	
OPLS	4.35	2.72	3.37	

<sup>a</sup> The values that are shown with nonbold font are the  $\chi^2$  values obtained after exclusion of the  ${}^3J(\text{H}_\text{N}, \text{H}_\alpha)$  coupling from the calculation.

pronounced differences in the various secondary structure populations. This is shown in Figure S2 of the Supporting Information which depicts the evolution of the cumulative Ramachandran plots (for the AMBER force field) as a function of simulation time: the general appearance of the plots remains pretty much identical, and it is only the detailed balance between the densities of the various secondary structure populations that gives rise to the observed  $\chi^2$  value variation.

**3.2. Ramachandran Plots, Secondary Structure Preferences, and the  $\chi^2$  Values.** The top row of Figure 2 shows the cumulative distributions of the peptide's ( $\varphi, \psi$ ) angles for the three force fields studied. In the light of accumulating evidence showing the preference of polyalanine for PPII-like structures,<sup>3,5,7,39–42</sup> the CHARMM force field clearly stands out as a putative outlier with its densely populated  $\alpha$ -helical region. This is in agreement with several previous studies<sup>5,9,10,35–38</sup> that have indicated this force field's  $\alpha$ -helical bias. AMBER and OPLS on the other hand appear rather similar: their most densely populated regions fall in the  $\beta$ -PPII part of the Ramachandran plot, with very little helical content. Their major difference lies in the clear separation (in the form of two discrete peaks) of the  $\beta$  and PPII regions in the case of AMBER, whereas OPLS gives a single elongated and asymmetric peak covering both the  $\beta$  and PPII areas. The difference Ramachandran plots, shown in the two lower rows of Figure 2, bring additional silent features of the force fields to light. For example, the alternating negative and positive peaks seen in the  $\beta$ -PPII area of the difference maps indicate the drift (to higher  $\varphi$  values) of the major PPII peak as we go from OPLS, to AMBER, to CHARMM. The positive peak centered on the borderline

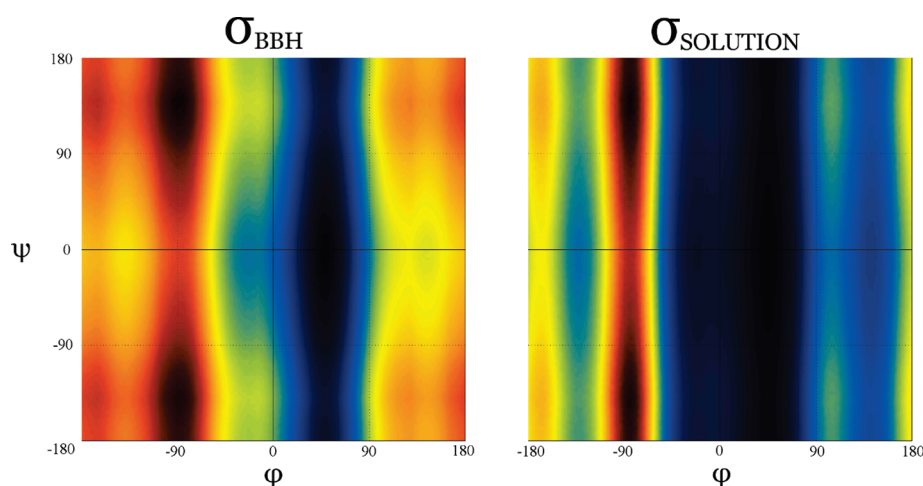
between  $\beta$  and PPII seen in the (OPLS – CHARMM) and (OPLS – AMBER) difference maps shows the significant population that OPLS has for conformations intermediate between  $\beta$  and PPII. Finally, in the PPII region of the (AMBER – CHARMM) and (OPLS – CHARMM) difference maps, the presence of a positive tail just above the major negative peaks indicates that CHARMM's major PPII population is shifted not only along  $\varphi$  but along lower  $\psi$  values as well.

Table 1 shows the  $\chi^2$  values obtained by comparing the simulation-derived  $J$ -couplings with the experimental values. Values are given for each of the three force fields as a function of (a) the three Karplus equation parameter sets and (b) the three sets of estimated errors for the calculated  $J$ -couplings<sup>7,9</sup> (the complete list of the  $J$ -coupling measurements used for calculating these  $\chi^2$  values can be found in Table S1 of the Supporting Information).

Even a cursory examination of Table 1 clearly shows that the tabulated  $\chi^2$  values create more questions than the answers they provide. The first question concerns the enormous variability of the  $\chi^2$  values. These range from 0.99 (for the AMBER–DFT1– $\sigma_{\text{BBH}}$  combination) to 9.60 (for the OPLS–DFT2– $\sigma_{\text{SOLUTION}}$  combination). The major source for this variability lies with the selection of error set, which is fully understandable given the progressive reduction of the estimated errors as we move from  $\sigma_{\text{BBH}}$ , to  $\sigma_{\text{X-RAY}}$ , to  $\sigma_{\text{SOLUTION}}$ . The  $\chi^2$  values obtained from the  $\sigma_{\text{SOLUTION}}$  set are so much larger than the other two sets that this set would appear to be an outlier. But, clearly, if the selection of a suitable set of estimated errors were to be performed on the basis of which set gives the lowest  $\chi^2$  values, this would only serve as an unequivocal demonstration of one's own biases. For this reason, a detailed discussion of the error sets and their effects (based on a reverse Monte Carlo approach) is presented in the section 3.3 that follows.

The second question concerns the apparent inconsistency between the  $\chi^2$  values of Table 1, the Ramachandran plots shown in Figure 2, and the (assumed) preference of polyalanine for PPII-like conformations. The most obvious example demonstrating this inconsistency concerns CHARMM's  $\chi^2$  values: this force field gives significantly lower values than OPLS (and in several cases even lower than AMBER's) although its Ramachandran plot is positively an outlier with its strong preference for  $\alpha$ -like conformations. Clearly, if the  $\chi^2$  values are insensitive to such outstanding differences in the ( $\varphi, \psi$ ) distributions, then their usefulness for force field development is diminished. We believe that the root of the problem lies with (a) the much tighter constraints that the experimental data pose on the  $\varphi$ -values, compared with the relatively few restraints for the  $\psi$ -angles and (b) the consistent overestimation of the  ${}^3J(\text{H}_\text{N}, \text{H}_\alpha)$  coupling demonstrated by both the OPLS and AMBER force fields (see below).

The third problem also concerns an apparent inconsistency between the  $\chi^2$  values and the Ramachandran plots, but this time the problem is not insensitivity but, rather, the hyper-sensitivity of the  $\chi^2$  values. To make this clear: OPLS and AMBER both populate mainly the PPII region, and their ( $\varphi, \psi$ ) distributions are rather similar (and strikingly different from CHARMM's). Still, the relatively small difference that is indeed present (namely, the  $\beta$ –PPII splitting observed with AMBER), leads to unexpectedly large differences in the  $\chi^2$  values, in some cases by as much as a factor of 2. The source of this problem lies mainly with the markedly asymmetric distribution of differences between the simulations and the experiment for the various types of  $J$ -couplings. This will be discussed at length in section 3.4, but in



**Figure 3.** Visualization of the effects of error set selection. These Ramachandran-like diagrams depict the cumulative log(probability) distributions of the peptide's ( $\varphi$ ,  $\psi$ ) angles based solely on the values of the experimental  $J$ -couplings and their corresponding estimated errors ( $\sigma_{\text{BBH}}$  and  $\sigma_{\text{SOLUTION}}$ , respectively) and were obtained through a reverse Monte Carlo procedure (see section 2.4 for details). For this calculation the DFT1 set of Karplus parameters has been used, and the number of Monte Carlo steps was 13.6 billion moves for each error set. The two diagrams are on the same arbitrary scale, and the linear color gradient ranges from dark blue (lowest probability), through yellow (intermediate values), to dark red (highest probability).

summary, OPLS (and to a lesser extent AMBER) appear to consistently and significantly overestimate the  ${}^3J(\text{H}_\text{N}, \text{H}_\alpha)$  coupling. This can clearly be seen from Table 1 (focusing on the values typeset in the nonbold font) where, for example, the DFT1– $\sigma_{\text{SOLUTION}}$  combination gave for OPLS (after exclusion of this coupling) a value for  $\chi^2$  of 2.72, significantly smaller from its original value of 6.86 using all data.

The last observation concerns the selection of parameter sets. Here a clear take-home message appears to be present: irrespective of the force field or error set selected, the DFT1 parameter set always results to a significantly better agreement with the experimental data. This is followed by the DFT2 and ORIG sets, with the exception of OPLS for which the ORIG set results to lower  $\chi^2$  values compared with the DFT2 set (noting, however, that this OPLS behavior changes and becomes identical with the other two force fields if the  ${}^3J(\text{H}_\text{N}, \text{H}_\alpha)$  coupling is excluded from the calculations).

Turning our attention to the force fields per se, we note the following: for the DFT1 set of parameters AMBER is consistently the best-performing force field, irrespective of the error set selected, reaching a value of  $\chi^2 = 0.99$  for the  $\sigma_{\text{BBH}}$  error set (identical with the one used by both Best et al.<sup>9</sup> and Wickstrom et al.<sup>11</sup>). For the ORIG and DFT2 parameters, CHARMM performs better than both AMBER and OPLS for  $\sigma_{\text{X-RAY}}$  and  $\sigma_{\text{SOLUTION}}$  but not for  $\sigma_{\text{BBH}}$  which favors AMBER. If the  ${}^3J(\text{H}_\text{N}, \text{H}_\alpha)$  coupling is excluded from the calculations, then AMBER is almost without exception the best-performing force field, followed this time by OPLS, and last CHARMM.

**3.3. On the Uncertainty of Estimated Errors.** The selection of a suitable set of estimated errors for the simulation-derived  $J$ -couplings is a consistent source of confusion in all recent literature concerning molecular dynamics studies of polyalanine. A seemingly incoherent mixing of parameters and estimated errors is the norm, as clearly revealed also by Table 1 of this paper where all combinations of parameters and error estimates have been presented (and treated) as if they were independent. In reality, of course, they are not independent. For example, the set of parameters denoted as ORIG by Best et al.,<sup>9</sup> Wickstrom et al.,<sup>11</sup> and this paper was derived by Hu and Bax<sup>30</sup> in their 1997

paper, and the estimated errors corresponding to this set of Karplus parameters is the one denoted as  $\sigma_{\text{SOLUTION}}$  in this communication (and not the  $\sigma_{\text{X-RAY}}$  or  $\sigma_{\text{BBH}}$  error sets). The confusion is further increased when the DFT1 and DFT2 sets of parameters enter the picture: for these two sets of parameters there are no published sets of corresponding estimated errors for the calculated  $J$ -couplings. Clearly, the absence of suitable error estimates for DFT1 and DFT2 is hardly a good reason for using any of the other available error sets (which were derived from different sets of parameters and through different parametrization procedures). Having noted these problems, however, does nothing for resolving the major question: are the simulations statistically consistent ( $\chi^2 \sim 1$ ,  $\sigma_{\text{BBH}}$ ) or almost certainly inconsistent ( $\chi^2 \sim 4$ ,  $\sigma_{\text{SOLUTION}}$ ) with the experiment?

To qualitatively tackle this problem we hypothesized that such large differences in the  $\chi^2$  values clearly imply the presence of very different restraints on the ( $\varphi$ ,  $\psi$ ) distribution maps, to the point that any error sets containing seriously underestimated errors could possibly be detected by the unreasonably tight ( $\varphi$ ,  $\psi$ ) distributions that would be required in order to obtain statistical consistency. To test this hypothesis, we performed a reverse Monte Carlo calculation as described in section 2.4 aiming to map on the ( $\varphi$ ,  $\psi$ ) plane the constraints imposed by the different error sets. This mapping involves no physical (e.g., force field-derived) restraints and is only based on the experimental data plus their estimated errors. The results from this calculation (for the  $\sigma_{\text{BBH}}$ –DFT1 and  $\sigma_{\text{SOLUTION}}$ –DFT1 combinations) are shown in Figure 3. The most notable feature of these diagrams is their indeterminacy along  $\psi$ , especially when the  $\sigma_{\text{SOLUTION}}$  set is used. The smearing of the probability distributions along  $\psi$  is a fair representation of the much reduced restraints (and, thus, information content) that the  $J$ -coupling data impose on this angle. It also partly explains the reason why CHARMM has such relatively low  $\chi^2$  values (especially with the  $\sigma_{\text{SOLUTION}}$  set; see Table 1) although it has such a pronounced  $\alpha$ -helical bias: the  $\varphi$  angles for both the  $\alpha$  and PPII populations of CHARMM are nearly identical (see Figure 2), making them (from the point of view of  $\chi^2$ ) equally consistent with most of the experimental restraints. The dip in probability separating the  $\beta$  and PPII areas

(most clearly seen as the red–blue–red stripes in the upper-left quadrant of the  $\sigma_{\text{SOLUTION}}$  distribution) partly explains the very high  $\chi^2$  values obtained for OPLS from the  $\sigma_{\text{SOLUTION}}$  set [and contributes to the low values obtained from CHARMM, since this force field does show the  $\beta$ –PPII splitting (Figure 2)].

Although the diagrams of Figure 3 are useful for visualizing some of the reasons behind the numerical results quoted in Table 1, they appear to be less useful for their intended usage, namely, to judge whether the  $\sigma_{\text{SOLUTION}}$  error set leads to an abnormally tight ( $\varphi, \psi$ ) distribution. Comparing these diagrams with the cumulative distributions obtained from the Protein Data Bank entries would suggest that the  $\sigma_{\text{SOLUTION}}$  error set does indeed lead to an unusually tight distribution along  $\varphi$ , especially when considering the pronounced minimum separating the  $\beta$  and PPII regions. On the other hand, the  $\sigma_{\text{SOLUTION}}$  map (and again only examining the projection along  $\varphi$ ) is not much tighter than the distributions obtained from the CHARMM and AMBER force fields for the given peptide (Figure 2). In summary, it would appear that even the most restrictive of the error sets available (i.e., the  $\sigma_{\text{SOLUTION}}$  set) cannot be excluded based solely on the tightness of the restraints it imposes on the ( $\varphi, \psi$ ) distribution. The only consistent way to obtain dependable error estimates appears to be a proper redetermination of the estimated errors based on statistical cross-validation methods.

**3.4. OPLS and AMBER Systematically Overestimate the  $^3J(\text{H}_{\text{N}}, \text{H}_{\alpha})$  Coupling.** The large  $\chi^2$  values obtained from OPLS, in combination (and in contrast) with its relatively reasonable Ramachandran plot, prompted us to examine the contribution of each type of  $J$ -coupling to the overall  $\chi^2$  value. To this end, we calculated  $\chi^2$  values for each [force field–parameter set–error set] combination after excluding one of each of the seven types of  $J$ -couplings. The results for all those combinations are given in Table S2 of the Supporting Information and clearly show that OPLS (and to a lesser extent AMBER) seriously overestimates the  $^3J(\text{H}_{\text{N}}, \text{H}_{\alpha})$  coupling. The differences between the experimental and simulation-derived values for this specific coupling are so large that the overall  $\chi^2$  are affected. For example, for the OPLS–DFT1– $\sigma_{\text{SOLUTION}}$  combination the  $\chi^2$  (upon exclusion of this coupling) changes from 6.86 to 2.72, for the OPLS–DFT2– $\sigma_{\text{SOLUTION}}$  from 9.60 to 3.37, for AMBER–DFT1– $\sigma_{\text{SOLUTION}}$  3.47  $\rightarrow$  1.73, etc. Even CHARMM shows a significant overestimation in some cases; for example, the CHARMM–DFT2– $\sigma_{\text{SOLUTION}}$  combination showed a reduction of the  $\chi^2$  value from 4.32 to 2.40. Exclusion of the specific  $J$ -coupling brings the Ramachandran plots of Figure 2 and the  $\chi^2$  values of Table 1 (nonbold font) in good agreement with each other and result to AMBER99SB appearing as the best-performing force field of those tested, followed by OPLS, and finally CHARMM. The finding that the agreement between the Ramachandran plots and the  $\chi^2$  values improves upon exclusion of this coupling should not be interpreted as a suggestion that this coupling should actually be excluded from any type of calculation. The contrary: what this analysis really shows is that valuable information which can lead to genuine force field improvement may be missed when focusing on global statistics instead of a meticulous examination of the agreement at the level of individual measurements.

## 4. DISCUSSION

We showed that 2  $\mu\text{s}$  long molecular dynamics simulations of hepta-alanine using the AMBER99SB force field appear to achieve full statistical consistency with the experimental  $J$ -couplings when

using established (from the literature) Karplus equation parameter and error sets. But this should not be considered the main finding of this communication. We believe that what these calculations really showed is that caution (if not skepticism) should be exercised even with such established measures of statistical agreement as the  $\chi^2$  value, especially in the absence of a validated set of estimated errors. To avoid biasing the errors toward the parameter set from which they were derived, the implementation of a proper statistically cross-validated procedure would be necessary.

But even if such a dependable set of estimated errors was available, we would still have to cautiously examine the information content of the experimental data: as the reverse Monte Carlo calculations showed, the currently available experimental data for hepta-alanine essentially constrain only the  $\varphi$  angle, making a global statistic (such as  $\chi^2$ ) unsuitable for even differentiating between force fields displaying as diverse secondary structure preferences as those displayed by CHARMM and OPLS. In the light of these findings, we sense that attempts to validate the various force fields using global statistics can only be taken as suggestive and that the emphasis should be shifted to quantifying the agreement between experiment and simulation on the level of individual experimental data.

## ■ ASSOCIATED CONTENT

**S Supporting Information.** Figure showing variation of the  $\chi^2$  values for the three force fields as a function of simulation time, figure showing cumulative Ramachandran plots vs simulation time, table of complete list of the  $J$ -coupling measurements from the molecular dynamics simulations, and table of the full set of  $\chi^2$  values after excluding one of each of the seven types of  $J$ -couplings. This material is available free of charge via the Internet at <http://pubs.acs.org>.

## ■ AUTHOR INFORMATION

### Corresponding Author

\*Phone: +30-25510-30620. Fax: +30-25510-30620. E-mail: glykos@mbg.duth.gr

## ■ REFERENCES

- (1) Dagget, V.; Kollman, P. A.; Kuntz, I. D. A Molecular Dynamics Simulation of Polyalanine: An Analysis of Equilibrium Motions and Helix–Coil Transitions. *Biopolymers* **1991**, *31*, 1115–1134.
- (2) Mu, Y.; Stock, G. Conformational Dynamics of Trialanine in Water: A Molecular Dynamics Study. *J. Phys. Chem. B* **2002**, *106*, 5294–5301.
- (3) Shi, Z.; Olson, C.; Rose, G.; Baldwin, R.; Kallenbach, N. Polyproline II Structure in a Sequence of Seven Alanine Residues. *Proc. Natl. Acad. Sci. U.S.A.* **2002**, *99*, 9190–9195.
- (4) Gnanakaran, S.; García, A. E. Validation of an All-Atom Protein Force Field: From Dipeptides to Larger Peptides. *J. Phys. Chem. B* **2003**, *107*, 12555–12557.
- (5) Gnanakaran, S.; García, E. Helix–Coil Transition of Alanine Peptides in Water: Force Field Dependence on the Folded and Unfolded Structures. *Proteins* **2005**, *59*, 773–782.
- (6) Hornak, V.; Abel, R.; Okur, A.; Strockbine, B.; Roitberg, A.; Simmerling, C. Comparison of Multiple Amber Force Fields and Development of Improved Protein Backbone Parameters. *Proteins* **2006**, *65*, 712–725.
- (7) Graf, J.; Nguyen, P. H.; Stock, G.; Schwalbe, H. Structure and Dynamics of the Homologous Series of Alanine Peptides: A Joint Molecular Dynamics/NMR Study. *J. Am. Chem. Soc.* **2007**, *129*, 1179–1189.

- (8) Altis, A.; Otten, M.; Nguyen, P. H.; Hegger, R.; Stock, G. Construction of the Free Energy Landscape of Biomolecules via Dihedral Angle Principal Component Analysis. *J. Chem. Phys.* **2008**, *128*, 245102/1–245102/11.
- (9) Best, R. B.; Buchete, N.-V.; Hummer, G. Are Current Molecular Dynamics Force Fields Too Helical? *Biophys. J.* **2008**, *95*, L07–L09.
- (10) Best, R. B.; Hummer, G. Optimized Molecular Dynamics Force Fields Applied to the Helix–Coil Transition of Polypeptides. *J. Phys. Chem. B* **2009**, *113*, 9004–9015.
- (11) Wickstrom, L.; Okur, A.; Simmerling, C. Evaluating the Performance of the ff99SB Force Field Based on NMR Scalar Coupling Data. *Biophys. J.* **2009**, *97*, 853–856.
- (12) Verbaro, D.; Ghosh, I.; Nau, W. M.; Schweitzer-Stenner, R. Discrepancies Between Conformational Distributions of a Polyalanine Peptide in Solution Obtained from Molecular Dynamics Force Fields and Amide I' Band Profiles. *J. Phys. Chem. B* **2010**, *114*, 17201–17208.
- (13) Palenčár, P.; Bleha, T. Molecular Dynamics Simulations of the Folding of Poly(alanine) Peptides. *J. Mol. Model.* **2011**, *9*, 2367–2374.
- (14) Karplus, M. Contact Electron-Spin Coupling of Nuclear Magnetic Moments. *J. Chem. Phys.* **1959**, *30*, 11–15.
- (15) Eising, A. A.; Hünenberger, P. H.; Krüger, P.; Mark, A. E.; Scott, W. R. P.; Tironi, I. G. *Biomolecular Simulation: The GROMOS96 Manual and User Guide*; Vdf Hochschulverlag, ETH Zürich: Zürich, Switzerland, 1996.
- (16) Koehl, P. Electrostatics Calculations: Latest Methodological Advances. *Curr. Opin. Struct. Biol.* **2006**, *16*, 142–151.
- (17) MacKerell, A. D.; Bashford, D.; Bellott, M.; Dunbrack, R. L.; Evanseck, J. D.; Field, M. J.; Fisher, S.; Gao, J.; Guo, H.; Ha, S.; McCarthy, J.; Kuchnir, L.; Kuczera, K.; Lau, F. T. K.; Mattos, C.; Michnick, S.; Ngo, T.; Nguyen, D. T.; Prodhom, B.; Reiher, W. E., III; Roux, B.; Schlenkrich, M.; Smith, J. C.; Stote, R.; Straub, J.; Watanabe, M.; Wiórkiewicz-Kuczera, J.; Yin, D.; Karplus, M. All-Atom Empirical Potential for Molecular Modelling and Dynamic Studies of Proteins. *J. Phys. Chem. B* **1998**, *102*, 3586–3616.
- (18) MacKerell, A. D.; Feig, M.; Brooks, C. L., III. Extending the Treatment of Backbone Energetics in Protein Force Fields: Limitations of Gas-Phase Quantum Mechanics in Reproducing Protein Conformational Distributions in Molecular Dynamics Simulations. *J. Comput. Chem.* **2004**, *25*, 1400–1415.
- (19) Jorgensen, W. L.; Maxwell, D. S.; Tirado-Rives, J. Development and Testing of the OPLS All-Atom Force Field on Conformational Energetics and Properties of Organic Liquids. *J. Am. Chem. Soc.* **1996**, *118*, 11225–11236.
- (20) Kaminski, G.; Friesner, R. A.; Tirado-Rives, J.; Jorgensen, W. L. Evaluation and Reparametrization of the OPLS-AA Force Field for Proteins via Comparison with Accurate Quantum Chemical Calculations on Peptides. *J. Phys. Chem. B* **2001**, *105*, 6474–6487.
- (21) Kale, L.; Skeel, R.; Bhandarkar, M.; Brunner, R.; Gursoy, A.; Krawetz, N.; Phillips, J.; Shinozaki, A.; Varadarajan, K.; Schulten, K. NAMD2: Greater Scalability for Parallel Molecular Dynamics. *J. Comput. Phys.* **1999**, *151*, 283–312.
- (22) Humphrey, W.; Dalke, A.; Schulten, K. VMD—Visual Molecular Dynamics. *J. Mol. Graphics* **1996**, *14*, 33–38.
- (23) Case, D. A.; Cheatham, T. E., III; Darden, T.; Gohlke, H.; Luo, R.; Merz, K. M., Jr.; Onufriev, A.; Simmerling, C.; Wang, B.; Woods, R. J. The Amber Biomolecular Simulation Programs. *J. Comput. Chem.* **2005**, *26*, 1668–1688.
- (24) Glykos, N. M. CARMA: A Molecular Dynamics Analysis Program. *J. Comput. Chem.* **2006**, *27*, 1765–1768.
- (25) Mu, Y.; Nguyen, P. H.; Stock, G. Energy Landscape of a Small Peptide Revealed by Dihedral Angle Principal Component Analysis. *Proteins* **2005**, *58*, 45–52.
- (26) Altis, A.; Nguyen, P. H.; Hegger, R.; Stock, G. Dihedral Angle Principal Component Analysis of Molecular Dynamics Simulations. *J. Chem. Phys.* **2007**, *126*, 244111/1–244111/10.
- (27) Frishman, D.; Argos, P. Knowledge-Based Protein Secondary Structure Assignment. *Proteins* **1995**, *23*, 566–579.
- (28) Kabsch, W.; Sander, C. Dictionary of Protein Secondary Structure: Pattern Recognition of Hydrogen-Bonded and Geometrical Features. *Biopolymers* **1983**, *22*, 2577–2637.
- (29) Joosten, R. P.; Te Beek, T. A.; Krieger, E.; Hekkelman, M. L.; Hooft, R. W.; Schneider, R.; Sander, C.; Vriend, G. A Series of PDB Related Databases for Everyday Needs. *Nucleic Acids Res.* **2011**, *39*, D411–D419.
- (30) Hu, J.-S.; Bax, A. Determination of  $\phi$  and  $\chi_1$  Angles in Proteins from  $^{13}\text{C}$ – $^{13}\text{C}$  Three-Bond  $J$  Couplings Measured by Three-Dimensional Heteronuclear NMR. How Planar Is the Peptide Bond? *J. Am. Chem. Soc.* **1997**, *119*, 6360–6368.
- (31) Hennig, M.; Bermel, W.; Schwalbe, H.; Griesinger, C. Determination of  $\psi$  Torsion Angle Restraints from  $^3J(C_{\alpha}C_{\alpha})$  and  $^3J(C_{\alpha}H^N)$  Coupling Constants in Proteins. *J. Am. Chem. Soc.* **2000**, *122*, 6268–6277.
- (32) Wirmer, J.; Schwalbe, H. Angular Dependence of  $^1J(N_{\beta}C_{\alpha i})$  and  $^2J(N_{\beta}C_{\alpha(i-1)})$  Coupling Constants Measured in  $J$ -Modulated HSQCs. *J. Biomol. NMR* **2002**, *23*, 47–55.
- (33) Ding, K.; Gronenborn, A. M. Protein Backbone  $^1\text{H}^N$ – $^{13}\text{C}^{\alpha}$  and  $^{15}\text{N}$ – $^{13}\text{C}^{\alpha}$  Residual Dipolar and  $J$  Couplings: New Constraints for NMR Structure Determination. *J. Am. Chem. Soc.* **2004**, *126*, 6232–6233.
- (34) Case, D. A.; Scheurer, C.; Bruschweiler, R. Static and Dynamic Effects on Vicinal Scalar  $J$  Couplings in Proteins and Peptides: A MD/DFT Analysis. *J. Am. Chem. Soc.* **2000**, *122*, 10390–10397.
- (35) Hegefelf, W. A.; Chen, S.-E.; DeLeon, K. Y.; Kuczera, K.; Jas, G. S. Helix Formation in a Pentapeptide: Experiment and Force-Field Dependent Dynamics. *J. Phys. Chem. A* **2010**, *114*, 12391–12402.
- (36) Freddolino, P. L.; Liu, F.; Gruebele, M.; Schulten, K. Ten-Microsecond Molecular Dynamics Simulation of a Fast-Folding WW Domain. *Biophys. J.* **2008**, *94*, L75–L77.
- (37) Mittal, J.; Best, R. B. Tackling Force-Field Bias in Protein Folding Simulations: Folding of Villin HP35 and Pin WW Domains in Explicit Water. *Biophys. J.* **2010**, *99*, L26–L28.
- (38) Matthes, D.; de Groot, B. L. Secondary Structure Propensities in Peptide Folding Simulations: A Systematic Comparison of Molecular Mechanics Interaction Schemes. *Biophys. J.* **2009**, *97*, 599–608.
- (39) Kameda, T.; Takada, S. Secondary Structure Provides a Template for the Folding of Nearby Polypeptides. *Proc. Natl. Acad. Sci. U.S.A.* **2006**, *103*, 17765–17770.
- (40) Kentsis, A.; Mezei, M.; Gindin, T.; Osman, R. Unfolded State of Polyalanine is a Segmented Polyproline II Helix. *Proteins* **2004**, *55*, 493–501.
- (41) Schweitzer-Stenner, R.; Measey, T.; Kakalis, L.; Jordan, F.; Pizzanelli, S.; Forte, C.; Griebenow, K. Conformations of Alanine-Based Peptides in Water Probed by FTIR, Raman, Vibrational Circular Dichroism, Electronic Circular Dichroism, and NMR Spectroscopy. *Biochemistry* **2006**, *46*, 1587–1596.
- (42) Woody, R. W. Circular Dichroism Spectrum of Peptides in the Poly(Pro)II Conformation. *J. Am. Chem. Soc.* **2009**, *131*, 8234–8245.